Full length article

Ab initio supported development of TiN/MoN superlattice thin films with improved hardness and toughness

Zecui Gao [a,*], Julian Buchinger [a], Nikola Koutná [a,b], Tomasz Wojcik [a], Rainer Hahn [a],
Paul Heinz Mayrhofer [a]

[a] *Institute of Materials Science and Technology, Technische Universität Wien, Getreidemarkt 9, Vienna 1060, Austria*
[b] *Department of Physics, Chemistry, and Biology (IFM), Linköping University, Linköping SE-58183, Sweden*

A R T I C L E   I N F O

A B S T R A C T

Motivated by density functional theory (DFT)-derived ductility indicators for face centered cubic (fcc, rocksalt) structured TiN/MoN$_{0.5}$ superlattices and Ti$_{0.5}$Mo$_{0.5}$N$_{0.75}$ solid solutions, TiN/MoN$_y$ superlattice (SL) thin films with bilayer periods Λ of 2.4, 3.9, 6.6, 9.9, and 23.0 nm and corresponding solid solutions were developed by DC reactive magnetron sputtering. These SLs allow for improved hardness H and critical fracture toughness K_{IC}, with both peaking at the same bilayer period Λ of 9.9 nm (where the MoN$_{0.5}$ layers crystallize with the ordered β-Mo$_2$N phase); $H = 34.8 \pm 1.6$ GPa and $K_{IC} = 4.1 \pm 0.2$ MPa$\sqrt{}$m. The correspondingly prepared fcc-Ti$_{0.5}$Mo$_{0.5}$N$_{0.77}$ solid solution has $H = 31.4 \pm 1.5$ GPa and $K_{IC} = 3.3 \pm 0.2$ MPa$\sqrt{}$m. Thus, especially the fracture toughness shows a significant superlattice effect. This is suggested by DFT—by the increase of the Cauchy pressure from -19 to $+20$ GPa for the 001-direction (while that in the 100-direction remained high, above 83 GPa) upon increasing Λ from 3 to 4 nm.

Together, experimental and computational investigations prove the importance of optimized bilayer periods for highest strength and fracture toughness, as well as optimized N-content for the solid solutions.

1. Introduction

Ceramic thin films (i.e., transition metal borides, carbides, nitrides, and oxides) deposited by physical vapor deposition (PVD), are renowned for their outstanding stiffness and hardness in the machining and forming tool industry [1–3]. Since hardness and fracture toughness are largely mutually exclusive, this means that ceramic thin films are severely compromised in many applications by a low intrinsic fracture toughness [4]. Therefore, significant research efforts are directed towards breaking down the adverse relationship [5]. The optimization of the fracture toughness has been further complicated by a lack of reliable testing methods. Lately, the development of *in situ* micromechanical testing methods—which usually involve the focused ion beam (FIB) machining of micropillars [6], clamped microbeams [7], or free-standing single-supported cantilevers [8] for example—has caused research activities on the fracture toughness of various thin films to surge.

Numerous strategies have been proposed to increase the resistance of ceramic films against crack propagation, including alloying with ductile phase toughening (e.g., Mo$_2$BC [9], and TiMeN [Me = Mo W, Nb, and Ta] [10]), nanostructure toughening (e.g., Ti-Si-N [11]), anion-vacancy-induced toughening (e.g., VMoN and VWN [12]), nano-multilayer/superlattice (SL) toughening [13–16], and toughening by optimizing the valence electron concentration [17,18]. Specifically, SLs, which are characterised by the alternating deposition of chemically disparate and structurally coherent nanolayers, have shown significant potential to simultaneously enhance the hardness and the fracture toughness of transition metal nitrides [13]. The so-called SL effect was first reported by Helmersson et al. [19] and Barnett and Madan [15,20], who showed that the hardness values of TiN/VN and TiN/NbN SL films considerably exceeds their constituent components. In both instances, the hardness also showed a clear dependence on the bilayer period Λ, i.e., the cumulative thickness of two adjacent layers in a SL. Chu and Barnett [21] proposed that such noticeable bilayer period-dependent hardness enhancement primarily originates from a hindrance of dislocation glide within SL layers and across interfaces, and/or the coherence strains in the interfaces as a result of the lat-

tice mismatch of the two components. Later, micromechanical cantilever bending tests on TiN/CrN [22], TiN/WN [23], and MoN/TaN [24] SLs showed that the SL effect could induce overlapping peaks of fracture toughness and hardness. The difference between the elastic moduli of the constituents was demonstrated to be an essential prerequisite for the SL effect in TiN/WN, which featured a significant shear modulus difference of 60 GPa, while the lattice mismatch was minimized [23]. The lattice mismatch (and thus coherency strains and/or misfit dislocations) was shown to enhance fracture toughness, but caused a weaker Λ dependence in the TiN/Cr$_{0.37}$Al$_{0.63}$N SLs, consisting of layers with almost identical shear moduli and a sizeable lattice mismatch [25].

Recently, high-throughput density functional theory (DFT) calculations of Koutná et al. [26] identified rocksalt-structured TiN/MoN$_{0.5}$ SLs (i.e., 50% vacancies on the N sublattice of the MoN layers) as a particularly promising system for simultaneous enhancement of hardness and toughness within the family of ceramic superlattice coatings. According to the authors, TiN/MoN$_{0.5}$ SL is chemically, mechanically, as well as dynamically stable, and offers excellent ductility, fracture toughness, as well as interfacial tensile strength. Similar to the TiN/WN$_{0.5}$ SL, TiN/MoN$_{0.5}$ SL features a very small lattice mismatch but largely disparate elastic moduli, which result in different dislocation line energies within the layers, thus, providing a good basis for the superlattice effect. Previous modeling and experimental results further suggest that face centered (fcc, rocksalt (NaCl) type with B1 cubic symmetry) MoN$_y$ can be stabilised by vacancies on the nitrogen sublattice [27,28].

PVD allows to synthesise various sub-nitrides of molybdenum, such as the high-temperature phase fcc γ-Mo$_2$N (having a nitrogen-deficient fcc lattice) and the low-temperature phase β-Mo$_2$N (having an ordered tetragonal lattice). Both phases exist over a wide range of stoichiometry MoN$_y$, with fcc γ-Mo$_2$N across the range from β-Mo$_2$N ($0.38 \leq y \leq 0.66$) to y values above 1 [29]. For nitrogen compositions y between 0.6 and 0.75, ordering of the nitrogen sublattice in γ-MoN$_y$ is energetically preferred, see Refs. [30,31], where this was conveniently noted as γ'-MoN$_y$.

In this combined experimental and computational work, we aim to expand the current understanding of nitrogen-vacancy-stabilized fcc structured TiN/MoN$_y$ ($y = 0.5$–0.7) superlattices, Ti$_{1-x}$Mo$_x$N$_y$ solid solutions (with $x \sim$0.5), and MoN$_y$ thin films. Additionally, the studied TiN/MoN$_y$ SL system provides further insight into the simultaneous toughening and hardening effect of the SL architecture on ceramic thin films. Our methods on the experimental side include X-ray diffraction, scanning electron microscopy, transmission electron microscopy, in-situ micromechanical experiments, and nanoindentation. The results are supported on the theoretical side by DFT calculations.

2. Experimental and computational details

2.1. Computational details

Density Functional Theory (DFT) calculations were carried out with the aid of the Vienna Ab-initio Simulation Package (VASP) [32,33] together with plane-wave projector augmented wave (PAW) pseudopotential [34] and the Perdew-Burke-Ernzerhof generalized gradient approximation (GGA) [35]. The plane-wave cut-off energy of 600 eV and the reciprocal space sampling with Γ-centered Monkhorst-Pack meshes [36] ensured a total energy accuracy of at least 10^{-3} eV/at. Equilibrium lattice constants of the face centered cubic rocksalt (Fm-3m) TiN and MoN structures were evaluated by fitting the minimum of the energy vs. volume curve. Additionally, the fcc MoN$_{0.75}$ and MoN$_{0.5}$ variants [37,38]—containing 25 and 50% of quasirandomly-distributed [39] N vacancies on the N sublattice—were considered. The fcc Ti$_{0.5}$Mo$_{0.5}$N$_y$ solid solutions, and 001-oriented fcc TiN/MoN$_y$ superlattices (fol-

lowing preferential orientation of our coatings, no other orientation was considered)—with Mo/(Ti+Mo) ratio, x, of 0.5 and $y = \{1, 0.75, 0.5\}$ (thus, featuring 0, 25, and 50% of N vacancies on the N sublattice)—were fully optimized by relaxing their volume, cell shape, and atomic positions. Relative chemical stability of the binaries (TiN, MoN$_y$), solid solutions (Ti$_{0.5}$Mo$_{0.5}$N$_y$), and superlattices (TiN/MoN$_y$) was estimated by calculating their formation energy,

$$E_f = (E_{tot} - n_{Ti}\mu_{Ti} - n_{Mo}\mu_{Mo} - n_N\mu_N)/(n_{Ti} + n_{Mo} + n_N) \qquad (1)$$

where E_{tot} is the total energy of the system, n_{Ti} (n_{Mo}, n_N) is the number of Ti (Mo, N) atoms, and μ_{Ti} (μ_{Mo}, μ_N) is the corresponding chemical potential, conventionally set to total energy per atom of the hexagonal close packed hcp-Ti (body centered cubic bcc-Mo, N$_2$ molecule). Mechanical stability [40] and elastic moduli were assessed from the elastic constants, calculated using the stress-strain approach [40,41]. The relative tendency for brittle/ductile behavior was estimated by calculating the Cauchy pressure, CP [10,42], defined as $CP = C_{12} - C_{44}$. Since fcc TiN/MoN$_y$ superlattices possess overall tetragonal elastic symmetry with more independent elastic constants (C_{11}, C_{33}, C_{12}, C_{23}, C_{44}, and C_{66}) than cubic systems (C_{11}, C_{12}, and C_{44}), one can introduce in-plane CP values ($CP_{100} = C_{23} - C_{44} = CP_{010} = C_{13} - C_{55}$) and out-of-plane CP values ($CP_{001} = C_{12} - C_{66}$) for our 001-oriented SLs, being indicators of in-plane and out-of-plane ductility, respectively. For these SLs, with tetragonal elastic symmetry, the homogenized CP values are obtained by averaging CP_{001}, CP_{100}, and CP_{010}. Additionally, the inherent tendency for brittleness/ductility [43] was estimated using the shear-to-bulk modulus ratio, G/B.

2.2. Coating deposition

Various Ti$_{1-x}$Mo$_x$N$_y$ solid solutions and TiN/MoN$_y$ superlattice (SL) thin films with bilayer periods (Λ) of 2.4, 3.9, 6.6, 9.9, and 23.0 nm were developed by a reactive unbalanced magnetron sputtering of one 3-inch Ti target and one 2-inch Mo target (99.99% purity for both, Plansee Composite Materials GmbH), in mixed Ar + N$_2$ atmospheres within an AJA Orion 5 system. After mounting the ultrasonically precleaned (in acetone and ethanol for 5 min each) polished single-crystalline Si (001-oriented, $20 \times 7 \times 0.38$ mm^3) and MgO (001-oriented, $10 \times 10 \times 0.50$ mm^3) substrates to a rotary substrate holder and evacuating the chamber to a base pressure of roughly 10^{-4} Pa, they were thermally cleaned at 400 °C (as obtained from calibration samples) for 20 min. However, the actual temperature during a deposition would be higher than 400 °C, due to the plasma irradiation. Afterwards, the substrates were Ar ion etched for 10 min by applying a DC potential of -750 V and using an Ar flow rate of 20 sccm at a pressure of 6 Pa.

The working gas pressure for all depositions was 0.4 Pa. The targets were DC-powered by ENI RPG-50 plasma generators, with a current density of 17.54 mA/cm^2 for the 3-inch Ti target (800 mA) and 25.46 mA/cm^2 for the 2-inch Mo target (500 mA). During a deposition, the substrates were DC biased with -50 V for a comparable dense growth morphology for all coatings. Four different MoN$_y$ coatings were synthesized by varying the nitrogen partial pressure with a flow rate ratio [f$_{N2}$= F$_{N2}$/(F$_{N2}$ + F$_{Ar}$)] variation from 0.2 to 0.5. As the sum of F$_{N2}$ + F$_{Ar}$ was kept constant with 10 sccm, the F$_{N2}$ was set to 2, 3, 4, or 5 sccm. This variation allowed us to identify the best f$_{N2}$ for the combination with TiN and the corresponding deposition rate, needed for controlled development of the SLs. All SLs were deposited with f$_{N2}$ = 0.3 (F$_{N2}$ =3 sccm and F$_{Ar}$ = 7 sccm). The N$_2$ partial pressure is 0.14 Pa, at this condition. The six different bilayer periods were realized through computer-controlled shutters above the Ti and Mo targets. The total deposition time was 222 min, to obtain $\sim$2 μm thick coatings.

For comparison, TiN, MoN$_y$, and Ti$_{1-x}$Mo$_x$N$_y$ solid solution thin films were prepared with identical conditions, powering of the tar-

gets (Ti target (800 mA) and Mo target (500 mA)), bias potential (−50 V), substrate temperature (400 °C), and f_{N2} = 0.3. Only for the $Ti_{1-x}Mo_xN_y$ solid solutions, the deposition time was reduced to 111 min as here the Ti and Mo targets were operated simultaneously, without shutter switching. To consider the higher N-consumption when powering the Ti and Mo sources simultaneously, one $Ti_{1-x}Mo_xN_y$ solid solution was also prepared with a higher f_{N2} of 0.5.

2.3. Chemical and structural characterization

All coatings were investigated by energy-dispersive X-ray spectroscopy (EDS, Philips XL30) to obtain their overall composition. Their crystal structures grown on Si and MgO substrates were analyzed by X-ray diffraction (XRD) in Bragg-Brentano configuration, featuring Cu K_α X-ray source (operated with 45 kV and 40 mA). Thicknesses and cross-sectional morphologies were studied by scanning electron microscopy (SEM), with an FEI Quanta 250, at an accelerating voltage of 10 kV. More detailed cross-sectional investigations of the microstructure were done by transmission electron microscopy (TEM, FEI TECNAI F20), at an acceleration voltage of 200 kV, combined with selected-area electron diffraction (SAED) analysis and scanning TEM (STEM) imaging.

2.4. Mechanical properties

Indentation hardness and modulus of the thin films grown on MgO were obtained using an ultra-micro indentation system (UMIS), equipped with a Berkovich diamond indenter tip [44–46]. The measurements were load-controlled, with forces ranging from 3 to 45 mN, and 31 indentations were carried out for each sample. We excluded the indentations exceeding an indentation depth of 10% of the coating thickness to avoid respectively minimize substrate interferences [47]. Measuring the curvature of coated MgO substrates was investigated by an optical profilometer (Nanovea PS50), and knowing the thickness of film and substrate, the biaxial modulus of the substrate, allows calculating the residual stresses using the Stoney equation formula given in [48].

The critical fracture toughness K_{IC} of the same films deposited on MgO is obtained through micromechanical bending tests. For this, free-standing microcantilevers were produced using a focused ion beam (FIB) system (FEI Quanta 200 3D featuring a Ga ion source) [25] Optimized geometries of cantilevers (dimensions of thickness w, breadth $b \approx w$, and length $l \approx 7w$) were machined using an ion beam current of 1.0 nA for coarse milling, and 0.5 nA for final cuts, at an acceleration voltage of 30 kV. On all cantilevers, a notch with depth a_0 of 300-500 nm (as shown in Fig. S1b) was milled with 50 pA. Small material bridges (50–100 nm wide) were left on both sides of the notch, to initiate the formation of a very sharp pre-crack at the notch base [49–51]. Notched cantilevers provide intrinsic toughness values of a material. Otherwise, due to the FIB preparation of the notch and the connected relatively large notch radius, the fracture toughness would be overestimated. For each coating sample, 6 microcantilevers were machined and tested (loading in the growth direction of the films). The bending tests were conducted with an *in-situ* SEM/FIB nanomechanical MEMS-based testing system (FT-NMT04, FemtoTools), equipped with a wedge-shaped diamond tip (10 μm width). The experiments were performed in displacement-controlled mode at 5 nm/s, loading until failure.

The critical fracture toughness, K_{IC}, is calculated as:

$$K_{IC} = f(a_0/w) \cdot F_m l / b w^{3/2} \tag{2}$$

where, F_m is the load at failure and l is the bending length from the notch to the point of force application. All other cantilever dimensions are defined in Fig. S1a. The dimensionless geometry factor $f(a_0/w)$–adopted from Matoy et al. [52] based on the work of Di Maio and Roberts [8]–can be obtained for our rectangular cantilevers by:

$$f(a_0/w) = 1.46 + 24.36(a_0/w) - 47.21(a_0/w)^2 + 75.18(a_0/w)^3 \tag{3}$$

As our micromechanical bending tests and the specimen geometries fulfil the traditional criteria associated with K_{IC}, we keep the subscripts "C" instead of "Q", which would indicate that the obtained values are only conditional. These criteria are that the sample dimension (w, a_0, and ligament size $w - a_0$) needs to be larger than the plastic zone (such as $a_0 \geq 2.5(K_{IC}/\sigma_y)^2$, with σ_y being the 0.2% yield strength) [53]. Using our results, presented later, and estimating σ_y with 1/3 of the hardness (according to the Tabor relation [54]) the a_0 values should be larger than 0.1–0.3 μm, which is the case for all of our samples yielding a_0 values in the range 0.3–0.5 μm.

The plane strain energy release rate G_C (in J/m2) for isotropic ideal brittle materials can be related to K_{IC} with:

$$G_C = K_{IC}^2 (1 - \nu^2)/E \tag{4}$$

For the Young's modulus E, we used the indentation modulus, and for the Poisson's ratio ν, we used the DFT-values (0.27 for TiN/MoN SLs with $\Lambda \approx 4$ nm, 0.23 for TiN, and 0.32 for $MoN_{0.5}$).

The fracture energy release rate J_n is calculated dividing the total strain energy with the fracture surface area under the notch after [55]:

$$J_n = \int F dx / b(w - a_0) \tag{5}$$

where, $\int F\, dx$ is the integral area under the load-deflection curve.

The experimental measurements are quoted based on the sample mean and standard deviation. For quantities derived from two or more independently measured attributes, error propagation is used to estimate the inaccuracy of the derived quantities.

3. Results and discussion

3.1. Ab initio studies

To support experimental investigations presented in the following sections, quantum-mechanical ab initio calculations were carried out. First, we estimated the relative chemical stability of TiN/MoN_y superlattices, their TiN and MoN_y building blocks, as well as $Ti_{0.5}Mo_{0.5}N_y$ solid solutions, all based on the face centered cubic (fcc) rocksalt (Fm-3m) phase. Consistently with preferential orientation of our coatings (discussed later), all computationally studied superlattices had (001) interfaces. The N substoichiometry (MoN_y, $y < 1$) was modeled via N vacancies, and motivated by the well-known thermodynamic driving force for vacancy formation in the fcc MoN [37,56,57]—often deposited in its $MoN_{0.5}$ variant [30,31]—as well as by chemical analysis of our own films (shown later). We note that various types of point defects unavoidably accompany physical vapor deposition processes. In particular, nitrogen vacancies are very common in the group 5 and 6 transition metal nitrides [58–60] due to their stabilisation effect on the cubic phase. As shown by Ozsdolay et al. [61] for epitaxial cubic MoN_x/MgO(001) layers, N vacancies may be also accompanied by metal vacancies. Contrarily, vacancies in TiN (group 4 nitride) are energetically unfavorable (see e.g., Fig. 6 in Ref. [62]). Furthermore, although various defect types should be anticipated in TiN/MoN SL films—following Ref. [61] a combination of N and Mo vacancies could be quite likely especially for MoN_x with $x = 0.75$ and 1—our idealised superlattice model assumes sharp interfaces and
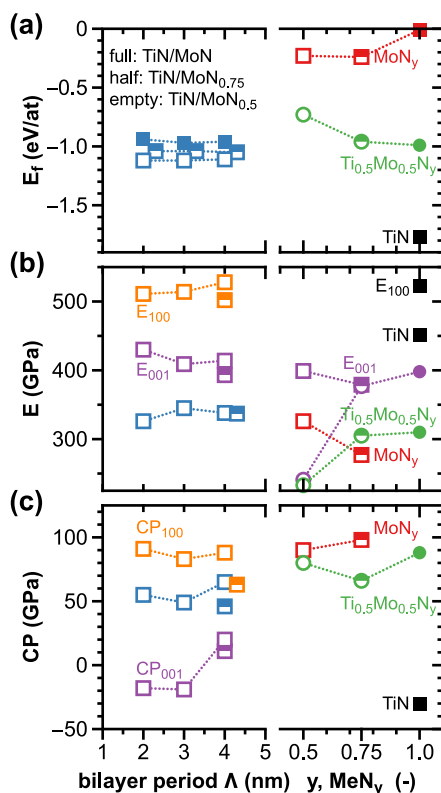
Fig. 1. Ab initio calculated formation energies E_f (a), Young's moduli (E, E_{100}, and E_{001}) (b) and Cauchy pressures (CP, CP_{100}, and CP_{001}) (c) for TiN, MoN_y, and $Mo_{0.5}Ti_{0.5}N_y$ solid solutions, as well as some TiN/MoN_y superlattices (with bilayer periods Λ of approx. 2, 3, and 4 nm). The orange and violet data points in panels (b, c) denote Young's moduli and Cauchy pressures in the [100] and [001] direction, i.e., in-plane and out-of-plane to interfaces of the superlattices, respectively. For fcc TiN, MoN_y, and $Mo_{0.5}Ti_{0.5}N_y$ solid solutions $E_{100} = E_{001}$ and $CP = CP_{100} = CP_{001}$. Full, half, and open symbols denote a N/Me ratio (N/Mo ratio), y, of 1, 0.75, and 0.5 for the fcc-binaries and solid solutions (TiN/MoN_y SLs), respectively.

non-metal vacancies in MoN layers as the *predominant* point defect type mainly responsible for the N substoichiometry (for illustration, see high energetic costs of Ti or N vacancies in TiN layers of TiN/WN SLs, in Ref. [23] Fig. 1).

For all the investigated bilayer periods, $\Lambda \approx \{2, 3, 4\}$ nm, DFT calculations, Fig. 1(a), suggest that TiN/MoN_y SLs energetically prefer to crystallise with 50% of N vacancies in fcc-MoN layers (note that the result for the lowest bilayer period has already been presented in Ref. [26]). Formation energies, E_f, of $TiN/MoN_{0.75}$ SLs lie about 0.08 eV/at higher, and those of defect-free TiN/MoN SLs show an even larger increase, by 0.15–0.18 eV/at, compared to their $TiN/MoN_{0.5}$ counterparts. Therefore, especially stabilisation of the fully stoichiometric SLs seems unlikely. Taking formation energy of a SL, E_f (SL), and subtracting formation energies of the corresponding building blocks, $1/2E_f$ (TiN) and $1/2E_f$ (MoN_y), we obtain the superlattice mixing enthalpy. For all the here studied SLs—out of which $TiN/MoN_{0.5}$ are the most relevant, as later underpinned also by evaluation of mechanical stability—their mixing enthalpy is slightly negative, varying between −0.05 and −0.09 eV/at, which is a sign of negligible energetic costs of interfaces. In fact, the negative mixing enthalpy even suggests an energetic gain. This indication is supported also by generally higher E_f of $Ti_{0.5}Mo_{0.5}N_y$ solid solutions, $y = \{1, 0.75, 0.5\}$, compared to $TiN/MoN_{0.75}$ and $TiN/MoN_{0.5}$ SLs. The $Ti_{0.5}Mo_{0.5}N_{0.5}$ variant, i.e., with 50% of vacancies on the N sublattice, is clearly energetically unfavorable, while $Ti_{0.5}Mo_{0.5}N_{0.75}$ and $Ti_{0.5}Mo_{0.5}N_{1.0}$ exhibit similar E_f values, suggest-

ing a fairly wide range of N stoichiometries ($0.75 \leq y \leq 1$) accessible experimentally (depending on the N_2 supply).

Evaluation of mechanical stability [40] based on elastic constants (listed in Table 1) confirms the well-known instability of the fcc (defect-free) MoN [63,64], while the vacancy-variants, $MoN_{0.75}$ and $MoN_{0.5}$ are stable in the fcc structure. Comparing the calculated C_{11} and C_{44} elastic constants with reference values for epitaxial cubic MoN_x/MgO(001) layers [61] yields a perfect agreement (only 6 GPa difference) between our DFT values for $MoN_{0.5}$ and measurements for $MoN_{0.69}$ (no experimental C_{ij} values for $MoN_{0.5}$ are available), whereas the DFT data for $MoN_{0.75}$ lie in-between those recorded for $MoN_{0.69}$ and $MoN_{0.75}$. Our calculations further indicate that the $Ti_{0.5}Mo_{0.5}N_y$ solid solutions, $y = \{1, 0.75, 0.5\}$, are mechanically stable, while the defect-free TiN/MoN SLs are unstable (or nearly unstable) for $\Lambda \approx \{2, 3\}$ nm ($\Lambda \approx 4$ nm) due to the negative (or only slightly positive) C_{44} elastic constant, indicating instability with respect to shearing. This is why we did not add this data set to Fig. 1b and c. The $TiN/MoN_{0.75}$ SL are mechanically stable for the largest investigated bilayer period, $\Lambda \approx 4$ nm, while the instability of the SLs with $\Lambda \approx \{2, 3\}$ nm—again due to negative C_{44} elastic constant—might be a consequence of small lateral sizes of our SL model enforcing rather ordered vacancy distributions. We note that increasing the N vacancy content at the N-sublattice in MoN layers from 25% ($TiN/MoN_{0.75}$) to 37.5% ($TiN/MoN_{0.625}$, not shown) increases the C_{44} elastic constant, hence, contributes to mechanical stabilisation of interfaces. The energetically most stable SLs, $TiN/MoN_{0.5}$, are predicted to be mechanically stable for all bilayer periods. The calculated elastic constants (see Table 1) were further used to estimate mechanical properties of selected (mechanically stable) systems. Specifically, Fig. 1b depicts the polycrystalline Young's moduli, E, together with their directional values in the [100] and [001] direction, E_{100} and E_{001}. Possessing cubic elastic symmetry, the binary (TiN, MoN_y) systems and $Ti_{0.5}Mo_{0.5}N_y$ solid solutions yield $E_{100} = E_{001}$, while the overall tetragonal SLs exhibit generally different E_{100} and E_{001} values, indicating differences between the in-plane (parallel to interfaces) vs. out-of-plane SL strength. Our DFT calculations ascribe the overall highest polycrystalline as well as directional Young's moduli to TiN ($E = 451$ GPa, $E_{100} = 523$ GPa), while both $MoN_{0.75}$ ($E = 277$ GPa, $E_{100} = 379$ GPa) and $MoN_{0.5}$ ($E = 326$ GPa, $E_{100} = 399$ GPa) yield significantly lower values. The E (E_{100}) moduli of $Ti_{0.5}Mo_{0.5}N_y$ decrease from 310 (398) down to 233 (241) GPa with y decreasing from 1 to 0.5, hence with decreasing the N sublattice occupancy. Similar to solid solutions, the $TiN/MoN_{0.5}$ SLs yield rather low polycrystalline E moduli (326–345 GPa). However, the predicted directional E_{001} values (409–430 GPa) exceed those of the solid solutions, and the E_{100} moduli (511–528 GPa) are almost as high as those of TiN, hence indicating high out-of-plane and even superior in-plane strength for the SLs.

Together with high strength, an essential prerequisite for superior fracture toughness is ductility. On the level of chemical bonding, the tendency for ductile behavior can be estimated by the Cauchy pressure, CP (Fig. 1c), and the shear-to-bulk modulus ratio, G/B (Table 1). According to Pettifor et al.'s [65] and Pugh's [43] criteria, a ductile material possesses $CP > 0$ and $G/B < 0.5$, respectively. Here CP and G/B values are not interpreted as strict boundaries between brittleness/ductility, but provide a relative comparison within fcc-based transition metal nitride materials. Fig. 1c compares the SL in-plane vs. out-of-plane ductility indicated by directional Cauchy pressures, CP_{100} and CP_{001}, respectively. The effective Cauchy pressure, CP, calculated as an average of CP_{100}, CP_{010} ($= CP_{100}$), and CP_{001}, gives a single homogenized value for the SL (note that $CP = CP_{100} = CP_{010} = CP_{001}$ for all other systems, i.e., with cubic elastic symmetry). With negative Cauchy pressure (−30 GPa) and $G/B = 0.66$, TiN exhibits the most brittle behavior of the considered systems. The $MoN_{0.75}$ and $MoN_{0.5}$, on the other

Table 1

Ab initio calculated formation energies, E_f (in eV/at), lattice parameters, a (in Å), elastic constants, C_{ij} (in GPa), polycrystalline bulk, shear, and Young's moduli, B, G, and E (all in GPa), directional Young's moduli and Cauchy pressures, $E_{[hkl]}$ and $CP_{[hkl]}$ (in GPa) for TiN, MoN$_y$, Ti$_{0.5}$Mo$_{0.5}$N$_y$, and TiN/MoN$_y$ superlattices (all with fcc respectively slightly tetragonal structure). Additionally, the shear-to-bulk modulus ratio, G/B, is given as well. The vacancy-free MoN is mechanically unstable; hence no elastic moduli are presented. The lattice parameter a of the SLs denotes the in-plane lattice parameter (a_{100}); we note that out-of-plane lattice parameters are slightly higher than in-plane values due to the Poisson's contraction, and they also vary depending on the distance from interfaces.

Systems	E_f	a_{100}	C_{11}	C_{12}	C_{13}	C_{33}	C_{44}	B	G	E	E_{100}	E_{001}	CP	CP_{100}	CP_{001}	G/B
TiN	−1.77	4.255	573	132	132	573	162	279	183	451	523	523	−30	−30	−30	0.66
MoN	−0.01	4.337	549	212	212	549	−43	–	–	–	–	–	–	–	–	–
MoN$_{0.75}$	−0.24	4.284	477	180	180	477	81	279	104	277	379	379	98	98	98	0.37
MoN$_{0.5}$	−0.23	4.202	508	196	196	508	106	300	124	326	399	399	90	90	90	0.41
Ti$_{0.5}$Mo$_{0.5}$N	−0.99	4.309	498	185	185	498	96	289	117	310	398	398	88	88	88	0.4
Ti$_{0.5}$Mo$_{0.5}$N$_{0.75}$	−0.96	4.254	463	165	165	463	99	264	116	305	377	377	66	66	66	0.44
Ti$_{0.5}$Mo$_{0.5}$N$_{0.5}$	−0.73	4.196	348	166	166	348	86	227	88	233	241	241	80	80	80	0.39
TiN/MoN$_{0.625}$, $_{\Lambda=2\,nm}$	−1.08	4.258	584	146	163	512	68	291	120	317	515	439	68	95	13	0.41
TiN/MoN$_{0.5}$, $\Lambda=2\,nm$	−1.12	4.250	576	133	161	503	70	285	124	326	511	430	91	91	−18	0.44
TiN/MoN$_{0.5}$, $\Lambda=3\,nm$	−1.12	4.248	582	132	167	487	84	287	133	345	514	409	83	83	−19	0.46
TiN/MoN$_{0.5}$, $\Lambda=4\,nm$	−1.12	4.248	601	141	173	495	85	296	129	338	528	414	88	88	20	0.44

hand, yield the overall highest CP (98 and 90 GPa for $y = 0.75$ and $y = 0.5$, respectively) and the lowest G/B values (0.37 and 0.41 for $y = 0.75$ and $y = 0.5$, respectively). The Ti$_{0.5}$Mo$_{0.5}$N$_y$ solid solutions are also identified as intrinsically ductile, yielding $G/B = 0.39$–0.44 and $CP = CP_{100}$ of 66–88 GPa, which exceeds DFT-calculated Cauchy pressure values of many transition metal nitrides, including ZrN, HfN, Ti$_{0.5}$M$_{0.5}$N with $M = $ [Hf, Ta, Cr], or Zr$_{0.5}$M$_{0.5}$N with $M = $ [Hf, Nb, V, Ta] (see Table 1 in Ref. [4]). Here, both ductility criteria point towards an increased ductile behavior with increasing N for $y \geq 0.75$ (from Ti$_{0.5}$Mo$_{0.5}$N$_{0.75}$ to Ti$_{0.5}$Mo$_{0.5}$N$_{1.0}$; the formation of Ti$_{0.5}$Mo$_{0.5}$N$_{0.5}$ is quite energetically unfavorable). Similar high Cauchy pressures are found in-plane for TiN/MoN$_{0.5}$ SLs ($CP_{100} = 83$–91 GPa), while the out-of-plane values, CP_{001}, reach only −19 to +20 GPa. Our calculations, therefore, indicate an excellent basis for SL in-plane plasticity in contrast to rather brittle behavior in the direction orthogonal to interfaces. The in-plane SL characteristics are relevant for, e.g., microcantilever bending experiments and nanoindentation, inducing local in-plane strains (e.g., sideways from the indenter), and any shear-loading during application (like during frictional contacts). Additionally, the considerable increase in CP_{001} from −19 to +20 GPa upon increasing Λ from 3 to 4 nm (while CP_{100} remains high) already hints towards an improved ductile behavior also out-of-plane for even larger bilayer periods.

We note that the above presented DFT results do not reflect important contributions to strength and ductility at the microscale, in particular, the material's microstructure. Furthermore, only SLs with low bilayer periods have been investigated so far, showing essentially no Λ-dependence of formation energies (e.g., E_f of different TiN/MoN$_{0.5}$ SLs varied by less than 0.01 eV/at), and a rather weak Λ-dependence of elastic properties, but a strong Λ-dependence for CP_{001} (for $\Lambda \geq 2$, as mentioned above). Small changes of the SL in-plane lattice parameter (which decreases from 4.250 Å to 4.234 Å for TiN/MoN$_{0.5}$ SLs with $\Lambda \approx 2$ nm and $\Lambda \approx 4$ nm), is also a sign for Λ-induced changes of interface strains. In order to reveal microstructural effects in TiN/MoN$_y$ SL films as well as to understand the role of the bilayer period (especially when increasing Λ beyond 4 nm), we further proceed with experimental results.

3.2. Composition and structure

Before developing TiN/MoN$_y$ SL thin films, we carefully analyzed the composition as well as structure of Mo-N coatings prepared with N$_2$ flow rate ratios, f$_{N2} = F_{N2}/(F_{Ar}+F_{N2})$, of 0.2, 0.3, 0.4, and 0.5. As proposed in previous works [27,28,30,66], the structure, phase stability, and mechanical properties of Mo-N highly depend on the N content. Independent on the N$_2$-supply during
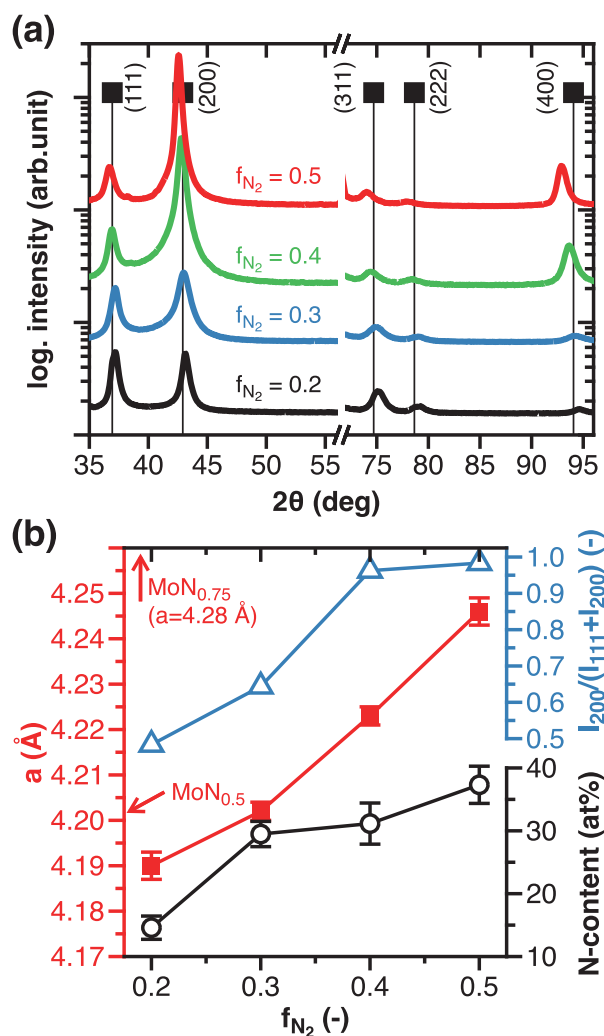

Fig. 2. XRD patterns **(a)** and lattice parameters (red line with full symbols), XRD peak intensity ratio [$I_{200}/(I_{111}+I_{200})$] (blue line with empty triangle symbols), and EDS-obtained nitrogen content **(b)** of MoN$_y$ coatings **(b)**, for the four N$_2$ flow rate ratios (f$_{N2}$) used. All on Si (001) substrates.

deposition, all Mo-N coatings are single-phase face centered cubic structured (fcc, B1, rocksalt), Fig. 2a, in accord to previous PVD studies. With increasing f$_{N2}$ from 0.2 to 0.5, the lattice parameter increases from 4.19 ± 0.01 to 4.24 ± 0.01 Å, and the peak intensity ratio [$I_{200}/(I_{111}+I_{200})$] increases from 0.48 to 0.98, respec-
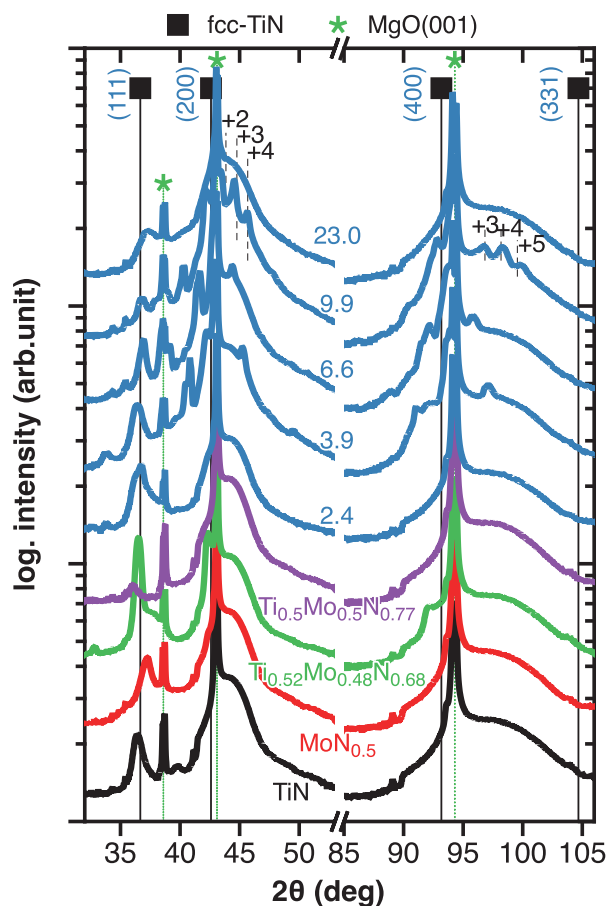
Fig. 3. XRD patterns of the TiN/MoN$_{0.5}$ SLs (labeled with the bilayer period in nm) and the monolithically grown TiN, MoN$_{0.5}$, and Ti$_{1-x}$Mo$_x$N$_y$ solid solutions (all grown on MgO (001) substrates). For the SLs with Λ = 3.9, 6.6 and 9.9 nm satellite peaks are clearly detectable, which are assigned for the Λ = 9.9 nm case.

Fig. 4. Lattice parameters a **(a)**, EDS-obtained N/metal ratio y **(b)** and Mo/(Mo+Ti) ratio x **(c)** of the superlattice TiN/MoN$_{0.5}$ coatings (averaged across all layers) and the monolithically grown TiN, MoN$_{0.5}$, and Ti$_{1-x}$Mo$_x$N$_y$ solid solutions (all grown on MgO (001) substrates). The crosses indicate the ab initio obtained lattice parameter (see Table 1), where the larger value for the Λ = 4 nm SL is for TiN/MoN$_{0.75}$ and the others are for TiN/MoN$_{0.5}$. The crosses for the Ti$_{0.5}$Mo$_{0.5}$N$_y$ solid solution cover the a range 4.254–4.309 Å valid for y = 0.75 and 1.0, respectively.

tively, Fig. 2b. Based on the comparison of the lattice parameter variation with DFT calculated lattice parameters for fcc-MoN$_y$ (4.28 Å for MoN$_{0.75}$ and 4.20 Å for MoN$_{0.5}$, marked in Fig. 2b) [37] and considering the qualitative EDS data (see Fig. 2b), we simply name the MoN$_y$ coatings prepared with f_{N2} = 0.3 and 0.5 as MoN$_{0.5}$ and MoN$_{0.75}$, respectively. We note, however, that the DFT model only assumes N vacancies, while also Mo vacancies may be present—as shown for epitaxial cubic MoN$_x$/MgO(001) layers [61]—which would affect lattice parameter values. In combination with our previous studies on TiN [11], f_{N2} = 0.3 was selected for the development of the monolithic TiN and MoN$_{0.5}$, and the SL films. To complement the study, also two Ti$_{1-x}$Mo$_x$N$_y$ solid solutions were prepared with f_{N2} = 0.3 and 0.5, which are named Ti$_{0.52}$Mo$_{0.48}$N$_{0.68}$ and Ti$_{0.5}$Mo$_{0.5}$N$_{0.77}$, respectively, based on their EDS-obtained Mo/(Ti+Mo) ratio, x, and N/metal ratio, y (shown later also in Fig. 4).

Based on the deposition rates obtained for the MoN$_{0.5}$ and TiN, TiN/MoN$_{0.5}$ SLs with similar MoN$_{0.5}$ and TiN layer thicknesses ℓ ($\ell_{TiN} \sim \ell_{MoN0.5}$) were developed. Their individual bilayer periods (2.4, 3.9, 6.6, 9.9, 23.0 nm) are simply estimated by dividing the total coating thickness by the total number of bilayers. Fig. 3 shows their XRD patterns together with those of TiN, MoN$_{0.5}$, and the Ti$_{0.52}$Mo$_{0.48}$N$_{0.68}$ and Ti$_{0.5}$Mo$_{0.5}$N$_{0.77}$ solid solutions grown on MgO (001) substrates. All coatings show a single-phase fcc structure with a strong (001) orientation, except for the Ti$_{0.52}$Mo$_{0.48}$N$_{0.68}$ solid solution, which shows a strong (111) XRD peak in addition. The TiN/MoN$_{0.5}$ SLs with Λ from 3.9 to 9.9 nm clearly exhibit satellite peaks (for example, the Λ = 9.9 SL), which illustrate sharp
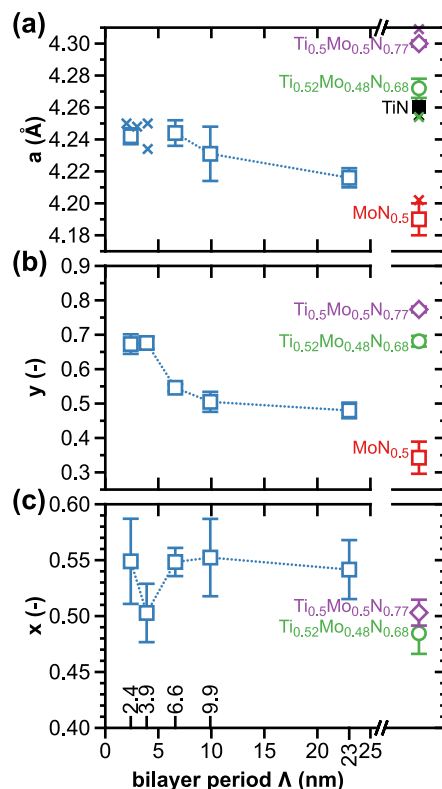
interfaces [67]. With increased Λ, these satellite peaks come closer to the main diffraction peak (200) [20], and higher-order satellite peaks are barely resolved [68]. For the SL with Λ = 23.0 nm, the satellite peaks are too close to the main peak, and for the SL with Λ = 2.4 nm, the individual TiN and MoN$_{0.5}$ layers are too thin to be resolved, therefore barely any satellite peaks can be observed for both of them. The XRD pattern of the SL with Λ = 2.4 nm is very comparable to those of the solid solutions Ti$_{0.52}$Mo$_{0.48}$N$_{0.68}$ and Ti$_{0.5}$Mo$_{0.5}$N$_{0.77}$. Because the individual satellite reflections of the SLs overlap with those from the ordered β-Mo$_2$N phase, the MoN$_{0.5}$ layers could also be present with this phase (which we actually proved by detailed SAED studies, presented later). Contrary to the XRD studies of the individual MoN$_y$ thin films (Fig. 2), which only showed a single-phase fcc-MoN$_y$ structure.

When the diffracting crystal planes are stacked with a small wavelength of sinusoidal modulation in atomic scattering factors and/or interplanar spacings, According to Eltoukhy and Greene [69], Λ can be calculated directly from the angular positions of the positive or negative satellites ($\theta_\pm$) relative to the Bragg angle (θ_B), by the formula:

$$\sin\theta_\pm = \sin\theta_B \pm m\lambda/2\Lambda \tag{7}$$

where λ is the X-ray wavelength, and m is the order of the superlattice reflection. Following this calculation, our TiN/MoN$_y$ SLs have modulation periods (Λ) of 2.8 $\pm$ 0.2, 3.9 $\pm$ 0.7, 6.1 $\pm$ 0.8, and 9.9 $\pm$ 0.7 nm, roughly in line with those estimated from the total coating thickness being 2.4, 3.9, 6.6, and 9.9 nm, respectively. For all samples, their negative satellite peaks are roughly similar in intensity to the positive ones, due to the similar X-ray scat-
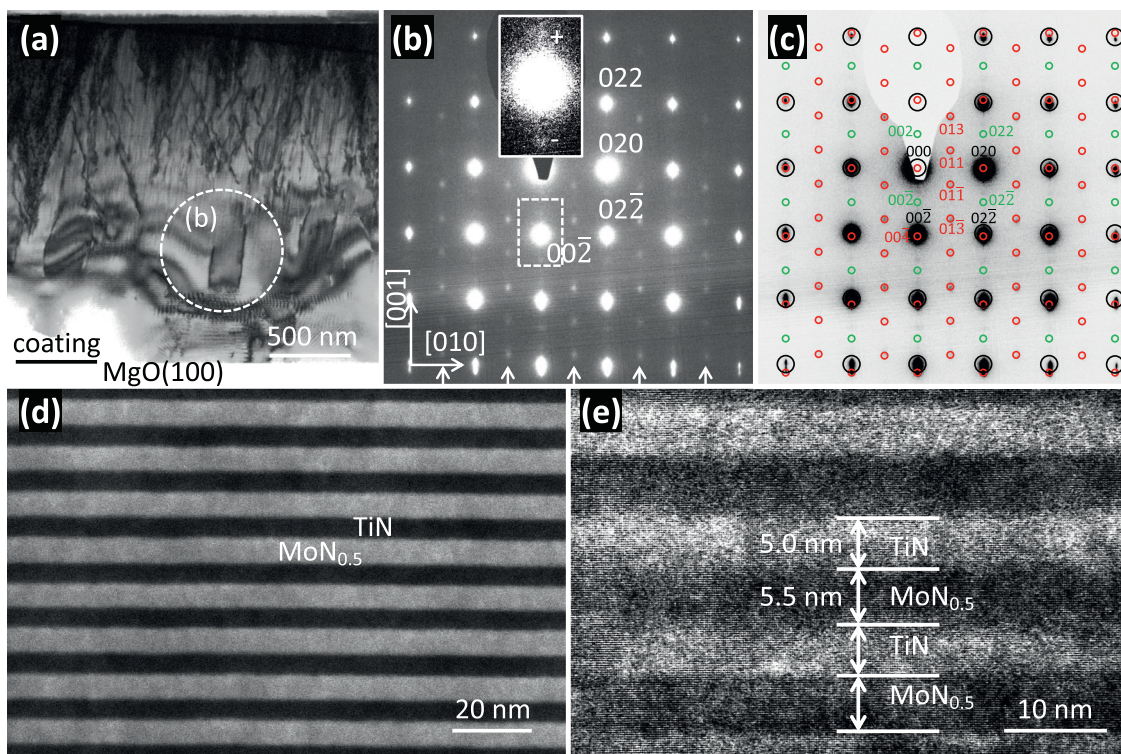
Fig. 5. Representative cross-sectional TEM images of the superlattice TiN/MoN$_{0.5}$ coatings using the sample with a bilayer period of 9.9 nm, on MgO (001) substrate. **(a)** Bright field overview image of the (100) cross section with indicated positions for the SAED pattern. **(b)** [100] SAED pattern with the most intense reflections from the rocksalt fcc TiN/MoN$_{0.5}$ lattice. Along [001], satellite reflections appear systematically due to the TiN/MoN$_{0.5}$ superlattice. These are marked by +/− in the enlargement of the area delimited by a white rectangular. The additional smaller reflections (along the columns marked with the small arrows) stem from the ordered tetragonal β-Mo$_2$N phase of the MoN$_{0.5}$ layers. **(c)** Simulated SAED pattern combining the reflections of TiN (larger black circles) and β-Mo$_2$N (smaller red and green circles) overlaid on the inverted SAED image from (b). **(d)** Detailed STEM image from the substrate near region. **(e)** Lattice-resolved high-resolution TEM micrograph.

tering factors and lattice spacings between fcc-MoN$_{0.5}$ and TiN [70]. The XRD patterns are used to obtain the lattice parameters, plotted in Fig. 4a. The N/metal ratio, y (Fig. 4b), using EDS obtained data, decreases with increased bilayer period, which fits the observed concomitant decreased lattice parameter. This decrease in y and a actually suggests that for small Λ values, the MoN$_y$ layers contain more N than for larger Λ values. Energetically, TiN/MoN$_{0.75}$ SLs are only slightly less preferred than TiN/MoN$_{0.5}$ SLs, and with $\Lambda = 4$ nm, the TiN/MoN$_{0.75}$ SL is already mechanically stable (Fig. 1 and Table 1). Additional DFT calculations proved that TiN/MoN$_{0.625}$ SLs are mechanically stable already for $\Lambda = 2$ nm. Thus, directly close to the TiN layers, the MoN$_y$ layers will have more N (supported by the surplus of N as the TiN layers would also grow stoichiometric with a lower f_{N2}). As with larger Λ, there are fewer interfaces and interface-near regions, the overall N-content decreases and also the lattice parameter ($a_{MoN0.5} < a_{MoN0.75}$).

The Mo/(Ti+Mo) ratios (x, obtained from the entire coating) are between 0.50 and 0.55 for all superlattices (Fig. 4c), hence, considering that the lattice parameter of MoN$_{0.5}$ (4.202 Å, DFT-data, Table 1) is slightly below that of TiN (4.242 Å literature data from JCPDF, or 4.255 Å, DFT-data, Table 1), $\ell_{MoN0.5}$ should be $\sim\ell_{TiN}$. Also, in-line with the N/metal ratio, Ti$_{0.5}$Mo$_{0.5}$N$_{0.77}$ exhibits a slightly larger lattice parameter than Ti$_{0.52}$Mo$_{0.48}$N$_{0.68}$.

Fig. 5 presents TEM and SAED images of the $\Lambda = 9.9$ nm TiN/MoN$_{0.5}$ superlattice grown on MgO (001). The TEM overview image (Fig. 5a) shows a dense growth morphology without an obvious columnar structure. The thickness of the TEM sample increases from the bottom (interface to the MgO (001) substrate) to the top, therefore especially at the top there is a higher density of strain-features present. The SAED pattern (Fig. 5b, projected

perpendicular to the [100] zone axis) shows an fcc structure with diffraction spot streaks (along [001]) due to the different lattice parameters along this direction of the individual TiN and MoN$_{0.5}$ layers. Additional smaller spots decorating the larger ones along this 001-direction (marked with + and – in the enlarged rectangle) indicate the superlattice structure, analogous to the observations by XRD. In Fig. 5c, this SAED image is overlaid with simulated SAED patterns of TiN (larger black circles) and the ordered tetragonal β-Mo$_2$N (smaller red and green circles). This clearly shows that within the 010-direction the lattice parameters of both structures are nearly identical, allowing for the excellent epitaxial growth, whereas along [001] the MoN$_{0.5}$ structure is slightly shorter with a c/a ratio of 1.96. Based on the comparison between measured and simulated SAED, the small reflections along the columns marked with arrows in Fig. 5b, clearly indicate that the MoN$_{0.5}$ layers crystallize with the ordered tetragonal β-Mo$_2$N phase.

The STEM image (Fig. 5d) shows the regular contrast modulation due to the alternating layering of TiN and MoN$_{0.5}$. Again, columns are not visible, only strain fields due to the epitaxial growth of the SL onto MgO (001). The individual layers are very flat with distinct interfaces to each other. The bright layers in this Z-contrast high angle annular dark-field (HAADF) image represent MoN$_{0.5}$, while the TiN layers yield a darker contrast due to their lower average atomic number. Contrary, the MoN$_{0.5}$ layers show darker contrast in the high-resolution TEM (HRTEM) image (Fig. 5e) because of the increased scattering of electrons. The continuous lattice fringes across various TiN and MoN$_{0.5}$ layers prove their high epitaxial relation. The slightly thicker MoN$_{0.5}$ layer ($\ell_{MoN0.5} = 5.5$ nm; $\ell_{TiN} = 5.0$ nm) is in-line with the Mo/(Ti+Mo) ratio of $x = 0.55$ for this coating. The slightly larger bilayer pe-

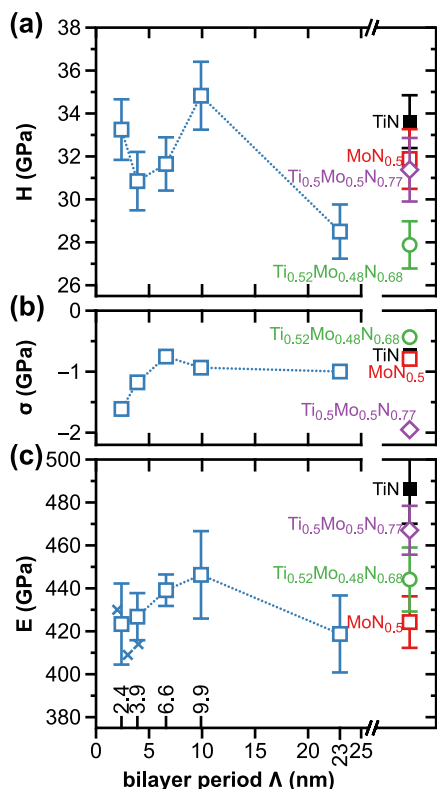**Fig. 6.** Indentation hardness H **(a)**, biaxial residual stress σ **(b)**, and indentation modulus E **(c)** of the TiN/MoN$_{0.5}$ SLs and the monolithically grown TiN, MoN$_{0.5}$, and Ti$_{1-x}$Mo$_x$N$_y$ solid solutions (all on MgO (001) substrates). The crosses indicate the ab initio obtained E_{100} moduli (compare Fig. 1 and Table 1).

3.3. Indentation hardness and modulus

The indentation hardness H of the TiN/MoN$_y$ SLs initially decreases from 33.3 ± 1.4 to 30.9 ± 1.4 GPa, with increasing Λ from 2.4 to 3.9 nm. After passing the valley, the hardness peaks at 34.8 ± 1.6 GPa (Λ = 9.9 nm), then, falling down to 28.8 ± 1.3 GPa (Λ = 23.0 nm), Fig. 6a. Comparing these data with those obtained from monolithically grown coatings suggest that there is not much deviation from a rule-of-mixture behavior between TiN and MoN$_{0.5}$, having 33.6 ± 1.2 and 31.9 ± 1.4 GPa, respectively. The hardness for TiN is very comparable to that of a previous study (31.7 ± 0.2 GPa [23]), which was also grown on MgO (001) using the same machine (but with a slightly lower bias of −40 V and a higher f_{N2} of 0.47 combined with a higher sputtering current of 1 A). The reported hardness for MoN$_y$ strongly depends on the chemical composition, where within single-phase fcc structured materials, the highest value of 33.0 ± 1.7 GPa is obtained for MoN$_{0.5}$ [28]. For higher and lower N contents, the hardness declines. For example, for ∼40 at% N (MoN$_{0.67}$, prepared at an N$_2$-to-total pressure ratio of 0.69), the hardness is 28.0 ± 2.0 GPa [28], which is very close to the value of our Ti$_{0.52}$Mo$_{0.48}$N$_{0.68}$ solid solution (27.9 ± 1.1 GPa), which was prepared with f_{N2} = 0.3. The higher N-containing solid solution, Ti$_{0.5}$Mo$_{0.5}$N$_{0.77}$ (prepared with f_{N2} = 0.5), presents a hardness of 31.4 ± 1.5 GPa, which is com-

parable to TiN and MoN$_{0.5}$, and also previously published data of Ti$_{1-x}$Mo$_x$N$_y$ coatings [71].

The comparison of the Λ = 23 nm SL with the monolithically grown films TiN, MoN$_{0.5}$, Ti$_{0.52}$Mo$_{0.48}$N$_{0.68}$ (f_{N2} = 0.3), and Ti$_{0.5}$Mo$_{0.5}$N$_{0.77}$ (f_{N2} = 0.5), as well as with the above-mentioned published H values for fcc-MoN$_y$—the highest value for MoN$_{0.5}$, which declines for higher and lower N content—suggests that this SL is composed of TiN and N-deficient fcc-MoN$_{0.5-z}$ [72]. The higher frequency of switching between Ti and Mo target for the SL with lower Λ can account for the less prone N$_2$-depletion of the working gas. Please see Fig. 2, showing that decreasing f_{N2} from 0.3 to 0.2 results in the formation of N-deficient fcc-MoN$_{0.5-z}$. Contrary, the chemistry of TiN is not that sensitive to f_{N2}.

The hardness of the SL with the smallest bilayer period of 2.4 nm is 33.2 ± 1.4 GPa and still between that of TiN and MoN$_{0.5}$. Reasons for the higher residual compressive stresses of this SL with Λ = 2.4 nm, Fig. 6b, can be interfacial effects, such as a higher contribution (due to more interfaces per coating thickness) from intermixed regions of adjacent layers, distorted metastable phases formed in the interface-near region, as well as oscillations of the d-spacings close to the interfaces [72,73]. The latter effects have been studied in detail by ab initio calculations of MoN-TaN superlattices [74]. Essentially, only the SL with Λ = 9.9 nm is harder than TiN while having the same compressive residual stresses of ∼−1 GPa but much lower indentation modulus, Fig. 6c.

The indentation modulus E of the SL coatings shows a comparable variation with the bilayer period as the hardness and peaks with 446 ± 20 GPa at Λ of 9.9 nm. Coherency strains by lattice-mismatched layers can cause increased elastic constants [75], explaining the initial increase in E with increasing Λ. The formation of misfit dislocations when exceeding a certain layer thickness will relax these strains, and thus the E declines again. The monolithic MoN$_{0.5}$ and TiN coatings yield E of 424 ± 12 GPa and 486 ± 16 GPa, respectively, is in reasonable agreement with previously published data of 430 ± 25 GPa for MoN$_{0.5}$ [30] and 452 ± 3 GPa for TiN [23]. The DFT calculated Young's moduli are E_{100} = 399 GPa for MoN$_{0.5}$ and E_{100} = 523 GPa for TiN, where the differences come from microstructural effects and other defects than N vacancies, in particular, also Mo vacancies could be present in the coatings and are disregarded by the model. Thus, both experiments and DFT calculations confirm that the layer materials for our superlattice coatings, MoN$_{0.5}$ and TiN, possess significantly different E moduli, while their lattice parameters are rather close with 4.20 Å for MoN$_{0.5}$ and 4.25 Å for TiN. According to previous literature reports, this provides a basis for increased resistance to dislocation motion across layers when the layers are thick enough for dislocations [21,76,77]. The Ti$_x$Mo$_{1-x}$N$_y$ solid solutions exhibit E values of 444 ± 15 GPa for Ti$_{0.52}$Mo$_{0.48}$N$_{0.68}$ and 467 ± 11 GPa for Ti$_{0.5}$Mo$_{0.5}$N$_{0.77}$, and are thus higher as those obtained by DFT for Ti$_{0.5}$Mo$_{0.5}$N$_{0.75}$ (E_{100} = 377 GPa) and Ti$_{0.5}$Mo$_{0.5}$N (E_{100} = 398 GPa). The DFT calculated polycrystalline Youngs' modulus for vacancy-free Ti$_{0.5}$Mo$_{0.5}$N is reported with 344 GPa [10], while we obtained E = 310 GPa (Table 1).

3.4. Fracture toughness evaluation

In Fig. S1a, a wedge indenter tip and a free-standing microcantilever are shown directly before testing. Figs. S1b through S1f depict the SEM micrographs of the fractured surface after bending testing for the SLs with increasing Λ from 2.4 to 23.0 nm, and those for TiN, MoN$_{0.5}$, and the Ti$_{0.5}$Mo$_{0.5}$N$_{0.77}$ solid solution are given in Fig. S1g, h, and i, respectively. These fracture cross sections show that only TiN exhibits a pronounced columnar growth morphology, whereas the other ones are very smooth and suggest very dense growth morphologies as proven by TEM investigations, as
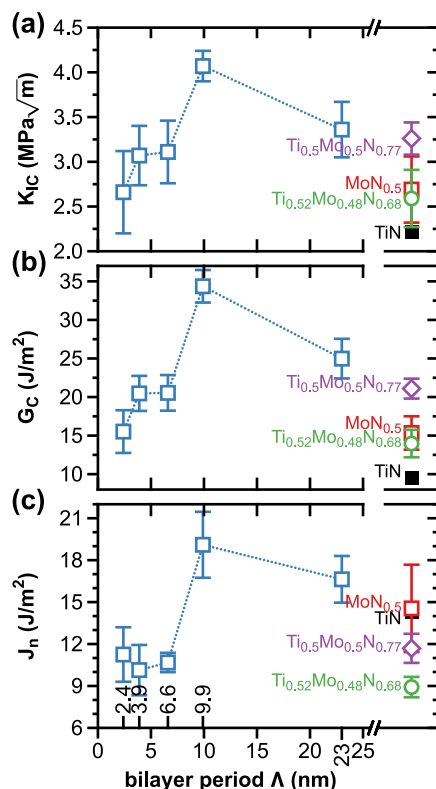
riod of 10.5 (instead of the 9.9 nm obtained from dividing the total coating thickness (from STEM) by the number of bilayers) agrees with the value obtained from the XRD satellite peak positions (9.9 ± 0.7 nm). Overall, the TEM analyses demonstrate that the TiN/MoN$_{0.5}$ superlattices on MgO (001) possess a high quality and a sharp compositional contrast at the interface, in excellent agreement with XRD investigations.

Fig. 7. Critical fracture toughness K_{IC} **(a)**, strain energy release rate G_C **(b)**, and fracture energy release rate J_n **(c)**, for the TiN/MoN$_y$ SLs and the monolithically grown TiN, MoN$_{0.5}$, and Ti$_{1-x}$Mo$_x$N$_y$ solid solutions (all on MgO (001) substrates).

shown in Fig. 5 for the SL with Λ = 9.9 nm. The fracture surfaces of all SLs and the MoN$_{0.5}$ and Ti$_{1-x}$Mo$_x$N$_y$ coatings do not show any evidence for a microstructure-related different crack-propagation. All cantilevers failed at the FIB-fabricated pre-notch, and all the initial thin material bridges and notch depths a_0 are visible in Fig. S1.

Representative load-deflection curves of all tested cantilevers are shown in Fig. S2a (presenting the SL coatings) and Fig. S2b (presenting the monolithically grown coatings). For TiN, only one cantilever is measured (therefore no error bar for the obtained values, which are presented later), which is in perfect agreement in H, E, and fracture toughness (K_{IC}) with previously published data [78]. All cantilevers provided perfectly linear load–deflection curves until fracture, but please be aware that their dimensions are different, and thus direct comparison of the individual load-deflection curves is not possible.

Contrary to the H and E dependence (Fig. 6), the fracture toughness K_{IC} of the SLs massively changes with the bilayer period and peaks at 4.1 $\pm$ 0.2 MPa$\sqrt{m}$ with Λ = 9.9 nm, Fig. 7a. The SL with the smallest bilayer period of 2.4 nm exhibits a K_{IC} of 2.7 $\pm$ 0.2 MPa$\sqrt{m}$, which is perfectly between those of TiN (2.2 MPa$\sqrt{m}$) and MoN$_{0.5}$ (2.8 $\pm$ 0.2 MPa$\sqrt{m}$). Opposed to this behavior, the SL with the largest bilayer period of 23.0 nm exhibits a K_{IC} of 3.4 $\pm$ 0.3 MPa$\sqrt{m}$, which is even above that of the Ti$_{0.5}$Mo$_{0.5}$N$_{0.77}$ solid solution (3.3 $\pm$ 0.2 MPa$\sqrt{m}$). The latter provided the highest K_{IC} value among the monolithically prepared coatings studied here. Interesting to note is also that the K_{IC} values nicely follow the DFT-derived ductility criteria combined with the E-moduli. These suggested, Fig. 1, increasing E-moduli and CP values with increasing N-content of the Ti$_{0.5}$Mo$_{0.5}$N$_y$ solid solution, in agreement with the increased K_{IC} values from Ti$_{0.52}$Mo$_{0.48}$N$_{0.68}$ to Ti$_{0.5}$Mo$_{0.5}$N$_{0.77}$. The ductility criteria also hint towards increasing

CP values for Λ above 4 nm, while at the same time, the E-moduli are not declining. In accord with the higher K_{IC} values for $\Lambda \geq$ 4 nm

The fracture toughness values of the TiN/MoN$_{0.5}$ SLs (with $\Lambda \geq$ 3.9 nm) and the N-rich solid solution, Ti$_{0.5}$Mo$_{0.5}$N$_{0.77}$, compare positively to those of other ceramic coatings (tested with the same machine and cantilever geometry), such as TiN/CrN SLs (peak of 2.0 $\pm$ 0.2 MPa$\sqrt{m}$ at Λ = 6.2 nm) [22], TiN/SiN$_x$ nanocomposite (~4.6 $\pm$ 0.6 MPa$\sqrt{m}$ at 8.5 at% Si) [79], Ti$_{0.54}$Al$_{0.46}$N (~3.5 $\pm$ 0.3 MPa$\sqrt{m}$) [80], as well as the Ti–X–C system (X = Ta, W, Nb, Mo, and V; ~ 2.0 MPa$\sqrt{m}$ [81]). Depending on the material-combination chosen to prepare superlattices, the so-called "superlattice effect" is sometimes more pronounced for lattice mismatched or shear modulus mismatched layers. For example, while a lattice mismatch only causes a mild superlattice effect on the fracture toughness for modulus-matched TiN/Cr$_{0.37}$Al$_{0.63}$N SLs (Δa = 0.14 Å), having a broad maximum at 2.5 $\pm$ 0.1 MPa$\sqrt{m}$ for Λ between 7.3 and 14 nm [25]; the modulus mismatch causes a pronounced superlattice effect for the lattice-matched TiN/WN SLs (ΔE_{100} = 67 GPa), exhibiting a peak with 4.6 $\pm$ 0.2 MPa$\sqrt{m}$ at Λ = 10.2 nm [23]. However, the TaN/MoN$_y$ SLs have a large lattice mismatch but similar shear moduli and still provide a distinct superlattice effect with a K_{IC} peak of 3.0 $\pm$ 0.2 MPa$\sqrt{m}$ at Λ = 5.2 nm [24]. The TiN/MoN$_{0.5}$ SLs studied here have a lattice mismatch (Δa = 0.05 Å) and a modulus mismatch (ΔG = 59 GPa), guaranteeing that their fracture toughness is noticeably dependent on the bilayer period and providing values above those of the monolithically prepared films.

The strain energy release rate G_C has the same trend as K_{IC}, Fig. 7b because the indentation modulus E only mildly varies with Λ. The G_C peak of 34.4 $\pm$ 2.1 J/m^2 for the SL with Λ = 9.9 nm is massively above that of the Ti$_{0.5}$Mo$_{0.5}$N$_{0.77}$ solid solution, which provides the highest value of 21.1 $\pm$ 1.3 J/m^2 among the monolithically grown coatings studied here (TiN, MoN$_{0.5}$, and Ti$_{1-x}$Mo$_x$N$_y$).

When comparing these experimental data (K_{IC} and G_C) with the DFT-derived intrinsic ductility criteria and E moduli, we find a good correlation between the SLs and solid solutions, where DFT only captured Λ values up to 4 nm. For such SLs, the ductility criteria are comparable to the Ti$_{0.5}$W$_{0.5}$N$_y$ solid solutions (Table 1), but their in-plane E moduli (E_{100}) are larger (with comparable out-of-plane values, E_{001}). The clearly enhance fracture toughness for the Λ = 9.9 nm SL—as compared to SLs with smaller Λ and the fcc-Ti$_{1-x}$Mo$_x$N$_y$ solid solutions—points towards the importance of dislocation activities, which do require a certain minimum layer thickness.

The fracture energy release rate J_n, calculated by dividing the area under the load-displacement curves with the corresponding fracture surface (Eq. (5)), is given in Fig. 7c. Although the SLs with Λ = 9.9 and 23.0 nm still provide much higher J_n values than the other SLs, their difference to TiN and MoN$_{0.5}$ is not that pronounced anymore (as was the case for K_{IC} and G_C). Also, the order within the monolithically grown coatings basically reversed (TiN and MoN$_{0.5}$ provide the highest J_n) values but basically lowest K_{IC} and G_C values, Fig. 7). This suggests that especially for TiN and MoN$_{0.5}$ the fracture surface seems to be more underestimated when simply using the projected area than it is for the other coatings and especially the SLs. In other words, the real fracture surface for TiN and MoN$_{0.5}$ is larger.

4. Summary and conclusions

We have developed highly 001-oriented fcc-structured TiN/MoN$_y$ SLs with bilayer period variations of Λ = 2.4, 3.9, 6.6, 9.9, and 23.0 nm as well as fcc-Ti$_{1-x}$Mo$_x$N$_y$ solid solutions (x ~0.5 and y ~0.75), to deepen current understanding of interface-

induced strengthening and toughening effects in TiN-based ceramic superlattices.

DFT calculations indicated that 001-oriented TiN/MoN_y SLs (with Λ = 2–4 nm) energetically prefer to crystallise with $\sim$50% of N vacancies in MoN_y layers (i.e., $MoN_{0.5}$), while the $Ti_{0.5}Mo_{0.5}N_y$ solid solutions were predicted to be the most energetically stable for $0.75 \leq y \leq 1$. Detailed XRD studies show that all SLs and solid solutions are single-phase fcc-structured, and the comparison with DFT-obtained lattice parameters (supported by EDS investigations) hints towards a composition according to $TiN/MoN_{0.5}$ and $Ti_{0.5}Mo_{0.5}N_{0.77}$. The SLs with Λ = 2.4 and 3.9 nm have higher N-contents and larger lattice parameters. Thus, their MoN_y layers are close to $MoN_{0.75}$ (DFT obtained lattice parameters for $MoN_{0.5}$ and $MoN_{0.75}$ are 4.202 and 4.284 Å, respectively).

On the nanoscale, intrinsic ductility criteria suggest excellent basis for plasticity for both $Ti_{0.5}Mo_{0.5}N_{0.75}$ solid solutions and $TiN/MoN_{0.5}$ SLs, while the later also show high elastic moduli (comparable even to TiN). In agreement with these, the SLs and $Ti_{0.5}Mo_{0.5}N_{0.77}$ outperform TiN during *in-situ* micromechanical bending tests yielding higher fracture toughness values K_{IC}. Especially, the latter shows a pronounced superlattice effect and peaks with 4.1 ± 0.2 MPa$\sqrt{m}$ at Λ = 9.9 nm. The other SLs are comparable to $Ti_{0.5}Mo_{0.5}N_{0.77}$ with K_{IC} $\sim$3.2 MPa$\sqrt{m}$, while TiN has only $\sim$2.2 MPa$\sqrt{m}$. The hardness of the SLs also peaks at Λ = 9.9 nm, but with H = 34.8 ± 1.6 GPa only slightly higher values are obtained than for TiN, $MoN_{0.5}$, and $Ti_{0.5}Mo_{0.5}N_{0.77}$ yielding 33.6 ± 1.2, 31.9 ± 1.4, and 31.4 ± 1.5 GPa, respectively. Detailed TEM and SAED studies of the 9.9-nm-SL showed that the $MoN_{0.5}$ layers crystallize with the ordered tetragonal β-Mo_2N phase in accord to DFT, which also yielded tetragonal distortion of the layers.

DFT not just guided the development of $TiN/MoN_{0.5}$ SLs with high fracture toughness and also helped to explain their lattice parameter and stoichiometry variation with the bilayer period. It also indicated the similarities between the low-bilayer-period SLs and the solid solutions and pointed towards increased ductility for bilayer periods beyond 4 nm.

Our studies furthermore showed that the epitaxial growth influences the preference for a certain crystal structure. While this might seem obvious it is rather interesting that the epitaxial growth of materials – which show perfect single-phase fcc structures with comparable lattice parameters ($\sim$4.25 Å for TiN and $\sim$4.20 Å for $MoN_{0.5}$) when grown independently – leads to different crystal structures. When grown onto fcc-TiN layers, the $MoN_{0.5}$ layers prefer to crystallize with the ordered tetragonal β-Mo_2N structure, which is rarely obtained especially when prepared by PVD at higher temperatures.

Data availability

The data that support the findings of this study are available from the authors on reasonable request.

Declaration of Competing Interest

The authors declare that they have no known competing or financial interests, or personal relationships, that could have influenced the work reported in this paper.

Acknowledgments

Supplementary materials

Supplementary material associated with this article can be found, in the online version, at doi:10.1016/j.actamat.2022.117871.

References

[1] P.H. Mayrhofer, C. Mitterer, L. Hultman, H. Clemens, Microstructural design of hard coatings, Prog. Mater. Sci. 51 (2006) 1032–1114, doi:10.1016/j.pmatsci.2006.02.002.

[2] A. Inspektor, P.A. Salvador, Architecture of PVD coatings for metalcutting applications: a review, Surf. Coat. Technol. 257 (2014) 138–153, doi:10.1016/j.surfcoat.2014.08.068.

[3] S. Veprek, M.J.G. Veprek-Heijman, Industrial applications of superhard nanocomposite coatings, Surf. Coat. Technol. 202 (2008) 5063–5073, doi:10.1016/j.surfcoat.2008.05.038.

[4] H. Kindlund, D.G. Sangiovanni, I. Petrov, J.E. Greene, L. Hultman, A review of the intrinsic ductility and toughness of hard transition-metal nitride alloy thin films, Thin Solid Films 688 (2019) 137479, doi:10.1016/j.tsf.2019.137479.

[5] D.G. Sangiovanni, Inherent toughness and fracture mechanisms of refractory transition-metal nitrides via density-functional molecular dynamics, Acta Mater. 151 (2018) 11–20, doi:10.1016/j.actamat.2018.03.038.

[6] M. Sebastiani, K.E. Johanns, E.G. Herbert, F. Carassiti, G.M. Pharr, A novel pillar indentation splitting test for measuring fracture toughness of thin ceramic coatings, Philos. Mag. 95 (2015) 1928–1944, doi:10.1080/14786435.2014.913110.

[7] B.N. Jaya, S. Bhowmick, S.A.S. Asif, O.L. Warren, V. Jayaram, Optimization of clamped beam geometry for fracture toughness testing of micron-scale samples, Philos. Mag. 95 (2015) 1945–1966, doi:10.1080/14786435.2015.1010623.

[8] D. Di Maio, S.G. Roberts, Measuring fracture toughness of coatings using focused-ion-beam-machined microbeams, J. Mater. Res. 20 (2005) 299–302, doi:10.1557/JMR.2005.0048.

[9] R. Soler, S. Gleich, C. Kirchlechner, C. Scheu, J.M. Schneider, G. Dehm, Fracture toughness of Mo2BC thin films: intrinsic toughness versus system toughening, Mater. Des. 154 (2018) 20–27, doi:10.1016/j.matdes.2018.05.015.

[10] D.G. Sangiovanni, V. Chirita, L. Hultman, Electronic mechanism for toughness enhancement in $Ti_xM_{1−x}N$ (M=Mo and W), Phys. Rev. B 81 (2010) 104107, doi:10.1103/PhysRevB.81.104107.

[11] M. Bartosik, R. Hahn, Z.L. Zhang, I. Ivanov, M. Arndt, P. Polcik, P.H. Mayrhofer, Fracture toughness of Ti-Si-N thin films, Int. J. Refract. Met. Hard Mater. 72 (2018) 78–82, doi:10.1016/j.ijrmhm.2017.12.015.

[12] K. Hanna, Toughness enhancement in hard single-crystal transition-metal nitrides: V-Mo-N and V-W-N alloys, PhD dissertation, Linköping University Electronic Press (2014). doi:10.3384/diss.diva-106472.

[13] M. Schlögl, C. Kirchlechner, J. Paulitsch, J. Keckes, P.H. Mayrhofer, Effects of structure and interfaces on fracture toughness of CrN/AlN multilayer coatings, Scr. Mater. 68 (2013) 917–920, doi:10.1016/j.scriptamat.2013.01.039.

[14] Z. Chen, M. Lou, D. Geng, Y.X. Xu, Q. Wang, J. Zheng, R. Zhu, Y. Chen, K.H. Kim, Effect of the modulation geometry on mechanical and tribological properties of TiSiN/TiAlN nano-multilayer coatings, Surf. Coat. Technol. 423 (2021) 127586, doi:10.1016/j.surfcoat.2021.127586.

[15] S. Barnett, A. Madan, Superhard superlattices, Phys. World 11 (1998) 45–48.

[16] A. Wagner, D. Holec, P.H. Mayrhofer, M. Bartosik, Enhanced fracture toughness in ceramic superlattice thin films: on the role of coherency stresses and misfit dislocations, Mater. Des. 202 (2021) 109517, doi:10.1016/j.matdes.2021.109517.

[17] T. Glechner, R. Hahn, T. Wojcik, D. Holec, S. Kolozsvári, H. Zaid, S. Kodambaka, P.H. Mayrhofer, H. Riedl, Assessment of ductile character in superhard Ta-C-N thin films, Acta Mater. 179 (2019) 17–25, doi:10.1016/j.actamat.2019.08.015.

[18] T. Glechner, S. Lang, R. Hahn, M. Alfreider, V. Moraes, D. Primetzhofer, J. Ramm, S. Kolozsvári, D. Kiener, H. Riedl, Correlation between fracture characteristics and valence electron concentration of sputtered Hf-C–N based thin films, Surf. Coat. Technol. 399 (2020) 126212, doi:10.1016/j.surfcoat.2020.126212.

[19] U. Helmersson, S. Todorova, S.A. Barnett, J.E. Sundgren, L.C. Markert, J.E. Greene, Growth of single-crystal TiN/VN strained-layer superlattices with extremely high mechanical hardness, J. Appl. Phys. 62 (1987) 481–484, doi:10.1063/1.339770.

[20] M. Shinn, L. Hultman, S.A. Barnett, Growth, structure, and microhardness of epitaxial Tin/Nbn superlattices, J. Mater. Res. 7 (1992) 901–911, doi:10.1557/Jmr.1992.0901.

[21] X. Chu, S.A. Barnett, Model of superlattice yield stress and hardness enhancements, J. Appl. Phys. 77 (1995) 4403–4411, doi:10.1063/1.359467.

[22] R. Hahn, M. Bartosik, R. Soler, C. Kirchlechner, G. Dehm, P.H. Mayrhofer, Superlattice effect for enhanced fracture toughness of hard coatings, Scr. Mater. 124 (2016) 67–70, doi:10.1016/j.scriptamat.2016.06.030.

[23] J. Buchinger, N. Koutná, Z. Chen, Z. Zhang, P.H. Mayrhofer, D. Holec, M. Bartosik, Toughness enhancement in TiN/WN superlattice thin films, Acta Mater. 172 (2019) 18–29, doi:10.1016/j.actamat.2019.04.028.

[24] R. Hahn, N. Koutná, T. Wójcik, A. Davydok, S. Kolozsvári, C. Krywka, D. Holec, M. Bartosik, P.H. Mayrhofer, Mechanistic study of superlattice-enabled high toughness and hardness in MoN/TaN coatings, Commun. Mater. 1 (2020) 62, doi:10.1038/s43246-020-00064-4.

[25] J. Buchinger, A. Wagner, Z. Chen, Z.L. Zhang, D. Holec, P.H. Mayrhofer, M. Bartosik, Fracture toughness trends of modulus-matched TiN/(Cr,Al)N thin film superlattices, Acta Mater. 202 (2021) 376–386, doi:10.1016/j.actamat.2020.10.068.

[26] N. Koutná, A. Brenner, D. Holec, P.H. Mayrhofer, High-throughput first-principles search for ceramic superlattices with improved ductility and fracture resistance, Acta Mater. 206 (2021) 116615, doi:10.1016/j.actamat.2020.116615.

[27] F.F. Klimashin, H. Euchner, P.H. Mayrhofer, Computational and experimental studies on structure and mechanical properties of Mo-Al-N, Acta Mater. 107 (2016) 273–278, doi:10.1016/j.actamat.2016.01.063.

[28] F.F. Klimashin, H. Riedl, D. Primetzhofer, J. Paulitsch, P.H. Mayrhofer, Composition driven phase evolution and mechanical properties of Mo–Cr–N hard coatings, J. Appl. Phys. 118 (2015) 025305, doi:10.1063/1.4926734.

[29] A.J. Perry, A.W. Baouchi, J.H. Petersen, S.D. Pozder, Crystal structure of molybdenum nitride films made by reactive cathodic arc evaporation, Surf. Coat. Technol. 54-55 (1992) 261–265, doi:10.1016/S0257-8972(09)90060-3.

[30] F.F. Klimashin, N. Koutna, H. Euchner, D. Holec, P.H. Mayrhofer, The impact of nitrogen content and vacancies on structure and mechanical properties of Mo-N thin films, J. Appl. Phys. (2016) 120, doi:10.1063/1.4966664.

[31] F. Anğay, L. Löfler, F. Tetard, D. Eyidi, P. Djemia, D. Holec, G. Abadias, Structure, stress, and mechanical properties of Mo-Al-N thin films deposited by dc reactive magnetron cosputtering: role of point defects, J. Vac. Sci. Technol. A 38 (2020) 053401, doi:10.1116/6.0000292.

[32] G. Kresse, D. Joubert, From ultrasoft pseudopotentials to the projector augmented-wave method, Phys. Rev. B 59 (1999) 1758–1775, doi:10.1103/PhysRevB.59.1758.

[33] G. Kresse, J. Furthmüller, Efficiency of ab-initio total energy calculations for metals and semiconductors using a plane-wave basis set, Comput. Mater. Sci. 6 (1996) 15–50, doi:10.1016/0927-0256(96)00008-0.

[34] W. Kohn, L.J. Sham, Self-consistent equations including exchange and correlation effects, Phys. Rev. 140 (1965) A1133, doi:10.1103/PhysRev.140.A1133.

[35] J.P. Perdew, K. Burke, M. Ernzerhof, Generalized gradient approximation made simple, Phys. Rev. Lett. 77 (1996) 3865–3868, doi:10.1103/PhysRevLett.77.3865.

[36] H.J. Monkhorst, J.D. Pack, Special points for Brillouin-zone integrations, Phys. Rev. B 13 (1976) 5188–5192, doi:10.1103/PhysRevB.13.5188.

[37] N. Koutná, D. Holec, O. Svoboda, F.F. Klimashin, P.H. Mayrhofer, Point defects stabilise cubic Mo-N and Ta-N, J. Phys. D Appl. Phys. 49 (2016), doi:10.1088/0022-3727/49/37/375303.

[38] A. Kirnbauer, A. Kretschmer, C.M. Koller, T. Wojcik, V. Paneta, M. Hans, J.M. Schneider, P. Polcik, P.H. Mayrhofer, Mechanical properties and thermal stability of reactively sputtered multi-principal-metal Hf-Ta-Ti-V-Zr nitrides, Surf. Coat. Technol. 389 (2020), doi:10.1016/j.surfcoat.2020.125674.

[39] S.H. Wei, L.G. Ferreira, J.E. Bernard, A. Zunger, Electronic properties of random alloys: special quasirandom structures, Phys. Rev. B 42 (1990) 9622–9649, doi:10.1103/PhysRevB.42.9622.

[40] F. Mouhat, F.X. Coudert, Necessary and sufficient elastic stability conditions in various crystal systems, Phys. Rev. B 90 (2014) 224104, doi:10.1103/PhysRevB.90.224104.

[41] R. Yu, J. Zhu, H.Q. Ye, Calculations of single-crystal elastic constants made simple, Comput. Phys. Commun. 181 (2010) 671–675, doi:10.1016/j.cpc.2009.11.017.

[42] H.Y. Niu, X.Q. Chen, P.T. Liu, W.W. Xing, X.Y. Cheng, D.Z. Li, Y.Y. Li, Extra-electron induced covalent strengthening and generalization of intrinsic ductile-to-brittle criterion, Sci. Rep. 2 (2012), doi:10.1038/srep00718.

[43] S.F. Pugh, Relations between the elastic moduli and the plastic properties of polycrystalline pure metals, Philos. Mag. 45 (1954) 823–843, doi:10.1080/14786440808520496.

[44] W.C. Oliver, G.M. Pharr, An improved technique for determining hardness and elastic modulus using load and displacement sensing indentation experiments, J. Mater. Res. 7 (1992) 1564–1583, doi:10.1557/JMR.1992.1564.

[45] S.M. Han, R. Saha, W.D. Nix, Determining hardness of thin films in elastically mismatched film-on-substrate systems using nanoindentation, Acta Mater. 54 (2006) 1571–1581, doi:10.1016/j.actamat.2005.11.026.

[46] A.C. Fischer-Cripps, Critical review of analysis and interpretation of nanoindentation test data, Surf. Coat. Technol. 200 (2006) 4153–4165, doi:10.1016/j.surfcoat.2005.03.018.

[47] R. Saha, W.D. Nix, Effects of the substrate on the determination of thin film mechanical properties by nanoindentation, Acta Mater. 50 (2002) 23–38, doi:10.1016/S1359-6454(01)00328-7.

[48] G.C.A.M. Janssen, M.M. Abdalla, F. van Keulen, B.R. Pujada, B. van Venrooy, Celebrating the 100th anniversary of the Stoney equation for film stress: developments from polycrystalline steel strips to single crystal silicon wafers, Thin Solid Films 517 (2009) 1858–1867, doi:10.1016/j.tsf.2008.07.014.

[49] S. Brinckmann, K. Matoy, C. Kirchlechner, G. Dehm, On the influence of micro-cantilever pre-crack geometries on the apparent fracture toughness of brittle materials, Acta Mater. 136 (2017) 281–287, doi:10.1016/j.actamat.2017.07.014.

[50] A. Riedl, R. Daniel, M. Stefenelli, T. Schöberl, O. Kolednik, C. Mitterer, J. Keckes, A novel approach for determining fracture toughness of hard coatings on the

[51] S. Brinckmann, C. Kirchlechner, G. Dehm, Stress intensity factor dependence on anisotropy and geometry during micro-fracture experiments, Scr. Mater. 127 (2017) 76–78, doi:10.1016/j.scriptamat.2016.08.027.

[52] K. Matoy, H. Schönherr, T. Detzel, T. Schöberl, R. Pippan, C. Motz, G. Dehm, A comparative micro-cantilever study of the mechanical behavior of silicon based passivation films, Thin Solid Films 518 (2009) 247–256, doi:10.1016/j.tsf.2009.07.143.

[53] A.K. Saxena, S. Brinckmann, B. Völker, G. Dehm, C. Kirchlechner, Experimental conditions affecting the measured fracture toughness at the microscale: notch geometry and crack extension measurement, Mater. Des. 191 (2020) 108582, doi:10.1016/j.matdes.2020.108582.

[54] J.R. Cahoon, W.H. Broughton, A.R. Kutzak, The determination of yield strength from hardness measurements, Metall. Trans. 2 (1971) 1979–1983, doi:10.1007/BF02913433.

[55] A.T. Zehnder, Fracture Mechanics, Springer Science+Business Media, 2012.

[56] K. Balasubramanian, L. Huang, D. Gall, Phase stability and mechanical properties of $Mo_{1-x}N_x$ with $0 \leq x \leq 1$, J. Appl. Phys. 122 (2017) 195101, doi:10.1063/1.4998686.

[57] F.F. Klimashin, L. Lobmaier, N. Koutná, D. Holec, P.H. Mayrhofer, The MoN–TaN system: role of vacancies in phase stability and mechanical properties, Mater. Des. 202 (2021) 109568, doi:10.1016/j.matdes.2021.109568.

[58] K. Balasubramanian, S.V. Khare, D. Gall, Energetics of point defects in rocksalt structure transition metal nitrides: thermodynamic reasons for deviations from stoichiometry, Acta Mater. 159 (2018) 77–88, doi:10.1016/j.actamat.2018.07.074.

[59] A.B. Mei, H. Kindlund, E. Broitman, L. Hultman, I. Petrov, J.E. Greene, D.G. Sangiovanni, Adaptive hard and tough mechanical response in single-crystal B1 VNx ceramics via control of anion vacancies, Acta Mater. 192 (2020) 78–88, doi:10.1016/j.actamat.2020.03.037.

[60] S. Karimi Aghda, D. Music, Y. Unutulmazsoy, H.H. Sua, S. Mráz, M. Hans, D. Primetzhofer, A. Anders, J.M. Schneider, Unravelling the ion-energy-dependent structure evolution and its implications for the elastic properties of (V,Al)N thin films, Acta Mater. 214 (2021) 117003, doi:10.1016/j.actamat.2021.117003.

[61] B.D. Ozsdolay, K. Balasubramanian, D. Gall, Cation and anion vacancies in cubic molybdenum nitride, J. Power Sources 705 (2017) 631–637, doi:10.1016/j.jallcom.2017.02.072.

[62] Z. Zhang, A. Ghasemi, N. Koutná, Z. Xu, T. Grünstäudl, K. Song, D. Holec, Y. He, P.H. Mayrhofer, M. Bartosik, Correlating point defects with mechanical properties in nanocrystalline TiN thin films, Mater. Des. 207 (2021) 109844, doi:10.1016/j.matdes.2021.109844.

[63] G.L.W. Hart, B.M. Klein, Phonon and elastic instabilities in MoC and MoN, Phys. Rev. B 61 (2000) 3151–3154, doi:10.1103/PhysRevB.61.3151.

[64] E.I. Isaev, S.I. Simak, I.A. Abrikosov, R. Ahuja, Y.K. Vekilov, M.I. Katsnelson, A.I. Lichtenstein, B. Johansson, Phonon related properties of transition metals, their carbides, and nitrides: a first-principles study, J. Appl. Phys. 101 (2007) 123519, doi:10.1063/1.2747230.

[65] D.G. Pettifor, M. Aoki, J.N. Murrell, A. Cottrell, A.M. Stoneham, R. Haydock, J.E. Inglesfield, J.B. Pendry, Bonding and structure of intermetallics: a new bond order potential, Philos. Trans. R. Soc. Lond. Ser. A Phys. Eng. Sci. 334 (1991) 439–449, doi:10.1098/rsta.1991.0024.

[66] I. Jauberteau, A. Bessaudou, R. Mayet, J. Cornette, J.L. Jauberteau, P. Carles, T. Merle-Méjean, Molybdenum nitride films: crystal structures, synthesis, mechanical, electrical and some other properties, Coatings 5 (2015), doi:10.3390/coatings5040656.

[67] A. Madan, Y.Y. Wang, S.A. Barnett, C. Engström, H. Ljungcrantz, L. Hultman, M. Grimsditch, Enhanced mechanical hardness in epitaxial nonisostructural Mo/NbN and W/NbN superlattices, J. Appl. Phys. 84 (1998) 776–785, doi:10.1063/1.368137.

[68] R.M. Fleming, D.B. McWhan, A.C. Gossard, W. Wiegmann, R.A. Logan, X-ray diffraction study of interdiffusion and growth in (GaAs)n(AlAs)m multilayers, J. Appl. Phys. 51 (1980) 357–363, doi:10.1063/1.327310.

[69] A.H. Eltoukhy, J.E. Greene, Compositionally modulated sputtered InSb/GaSb superlattices: crystal growth and interlayer diffusion, J. Appl. Phys. 50 (1979) 505–517, doi:10.1063/1.325643.

[70] D. Holec, M. Friak, J. Neugebauer, P.H. Mayrhofer, Trends in the elastic response of binary early transition metal nitrides, Phys. Rev. B 85 (2012) 9, doi:10.1103/PhysRevB.85.064101.

[71] Q. Yang, L.R. Zhao, P.C. Patnaik, X.T. Zeng, Wear resistant TiMoN coatings deposited by magnetron sputtering, Wear 261 (2006) 119–125, doi:10.1016/j.wear.2005.07.008.

[72] Z. Zhang, X. Gu, D. Holec, M. Bartosik, P.H. Mayrhofer, H.P. Duan, Superlattice-induced oscillations of interplanar distances and strain effects in the CrN/AlN system, Phys. Rev. B 95 (2017) 155305, doi:10.1103/PhysRevB.95.155305.

[73] N. Koutna, P. Rehak, Z. Chen, M. Bartosik, M. Fallmann, M. Cerny, Z. Zhang, M. Friak, M. Sob, P.H. Mayrhofer, D. Holec, Correlating structural and mechanical properties of AlN/TiN superlattice films, Scr. Mater. 165 (2019) 159–163, doi:10.1016/j.scriptamat.2019.02.021.

[74] N. Koutná, D. Holec, M. Friák, P.H. Mayrhofer, M. Šob, Stability and elasticity of metastable solid solutions and superlattices in the MoN-TaN system: first-principles calculations, Mater. Des. 144 (2018) 310–322, doi:10.1016/j.matdes.2018.02.033.

[75] A.F. Jankowski, T. Tsakalakos, The effect of strain on the elastic constants of noble metals, J. Phys. F Met. Phys. 15 (1985) 1279 0305-4608/15/i=6/a=013.

[76] J.S. Koehler, Attempt to design a strong solid, Phys. Rev. B 2 (1970) 547–551, doi:10.1103/PhysRevB.2.547.

[77] J.W. Gahn, Hardening by spinodal decomposition, Acta Metall. 11 (1963) 1275–1282, doi:10.1016/0001-6160(63)90022-1.

[78] A.N. Wang, G.P. Yu, J.H. Huang, Fracture toughness measurement on TiN hard coatings using internal energy induced cracking, Surf. Coat. Technol. 239 (2014) 20–27, doi:10.1016/j.surfcoat.2013.11.010.

[79] M. Sperr, Z.L. Zhang, Y.P. Ivanov, P.H. Mayrhofer, M. Bartosik, Correlating elemental distribution with mechanical properties of TiN/SiNx nanocom-posite coatings, Scr. Mater. 170 (2019) 20–23, doi:10.1016/j.scriptamat.2019.05.020.

[80] W.M. Seidl, M. Bartosik, S. Kolozsvári, H. Bolvardi, P.H. Mayrhofer, Influence of Ta on the fracture toughness of arc evaporated Ti-Al-N, Vacuum 150 (2018) 24–28, doi:10.1016/j.vacuum.2018.01.028.

[81] M. Bielawski, K.Y. Chen, Computational evaluation of adhesion and mechanical properties of nanolayered erosion-resistant coatings for gas turbines, J. Eng. Gas. Turbines Power (2011) 133, doi:10.1115/1.4002158.